SCIENTIFIC DATA

OPEN

DATA DESCRIPTOR

Received: 11 December 2018
Accepted: 17 April 2019
Published online: 27 May 2019

The FLUXCOM ensemble of global land-atmosphere energy fluxes

Martin Jung[1], Sujan Koirala[1], Ulrich Weber[1], Kazuhito Ichii[2,3], Fabian Gans[1], Gustau Camps-Valls[4], Dario Papale[5], Christopher Schwalm[6], Gianluca Tramontana[5] & Markus Reichstein[1]

Although a key driver of Earth's climate system, global land-atmosphere energy fluxes are poorly constrained. Here we use machine learning to merge energy flux measurements from FLUXNET eddy covariance towers with remote sensing and meteorological data to estimate global gridded net radiation, latent and sensible heat and their uncertainties. The resulting FLUXCOM database comprises 147 products in two setups: (1) 0.0833° resolution using MODIS remote sensing data (RS) and (2) 0.5° resolution using remote sensing and meteorological data (RS + METEO). Within each setup we use a full factorial design across machine learning methods, forcing datasets and energy balance closure corrections. For RS and RS + METEO setups respectively, we estimate 2001–2013 global (±1 s.d.) net radiation as 75.49 ± 1.39 W m^{-2} and 77.52 ± 2.43 W m^{-2}, sensible heat as 32.39 ± 4.17 W m^{-2} and 35.58 ± 4.75 W m^{-2}, and latent heat flux as 39.14 ± 6.60 W m^{-2} and 39.49 ± 4.51 W m^{-2} (as evapotranspiration, 75.6 ± 9.8 × 10^3 km^3 yr^{-1} and 76 ± 6.8 × 10^3 km^3 yr^{-1}). FLUXCOM products are suitable to quantify global land-atmosphere interactions and benchmark land surface model simulations.

Background & Summary

Intercomparisons of global land surface models (LSMs) suggest large uncertainties regarding magnitude and pattern of land-atmosphere energy fluxes[1,2], making it difficult to assess and close energy and water budgets[3–5]. Existing regional networks of *in-situ* measurements from FLUXNET eddy covariance towers[6] provide only unevenly spaced point information impairing direct comparisons with LSMs. In addition, the lack of energy balance closure of around 20% across sites suggests systematic biases of measured turbulent latent and sensible heat fluxes[7]. The reasons for the energy balance closure gap are unclear and a community-accepted correction is unavailable.

Previous efforts to integrate FLUXNET measurements, satellite remote sensing and climate data with machine learning[8–10] have yielded global products of land-atmosphere fluxes that have been used frequently to evaluate LSM simulations[11–15], for water budgets[16,17], and land-atmosphere interactions[18–21]. However, data-driven global flux estimates are subject to uncertainty from, for example, choice in machine learning algorithm and predictor variables, global climate forcing data, and the lack of energy balance closure. A better characterisation of these uncertainties is needed for energy and water budget studies and to interpret apparent mismatches with LSM simulations. This, in turn, will lead to improvements of global estimation of land-atmosphere energy fluxes by data-driven and process models.

The FLUXCOM initiative (www.fluxcom.org) aims to improve our understanding of the multiple sources and facets of uncertainties in empirical upscaling and, ultimately, to provide an ensemble of machine learning-based global flux products to the scientific community. We use two complementary experimental setups of input drivers (covariates) and resulting global gridded products. In the remote sensing ("RS") setup, fluxes are estimated exclusively from Moderate Resolution Imaging Spectroradiometer (MODIS) satellite data. The second approach additionally includes meteorological information. In this "RS + METEO" setup, fluxes are estimated from daily

[1]Max Planck Institute for Biogeochemistry, Hans-Knöll-Str. 10, 07745, Jena, Germany. [2]Center for Environmental Remote Sensing, Chiba University, 1-33, Yayoi-cho, Inage-ku, Chiba, 236-0001, Japan. [3]Center for Global Environmental Research, National Institute for Environmental Studies, 16-2, Onogawa, Tsukuba, 305-0053, Japan. [4]Image Processing Laboratory (IPL), C/Catedrático José Beltrán, 2. 46980 Paterna, Universitat de València, València, Spain. [5]University of Tuscia DIBAF, Via C. de Lellis snc, 01100, Viterbo, Italy. [6]Woods Hole Research Center, 149 Woods Hole Road, Falmouth, MA, 02540-1644, USA. Correspondence and requests for materials should be addressed to M.J. (email: mjung@bgc-jena.mpg.de)

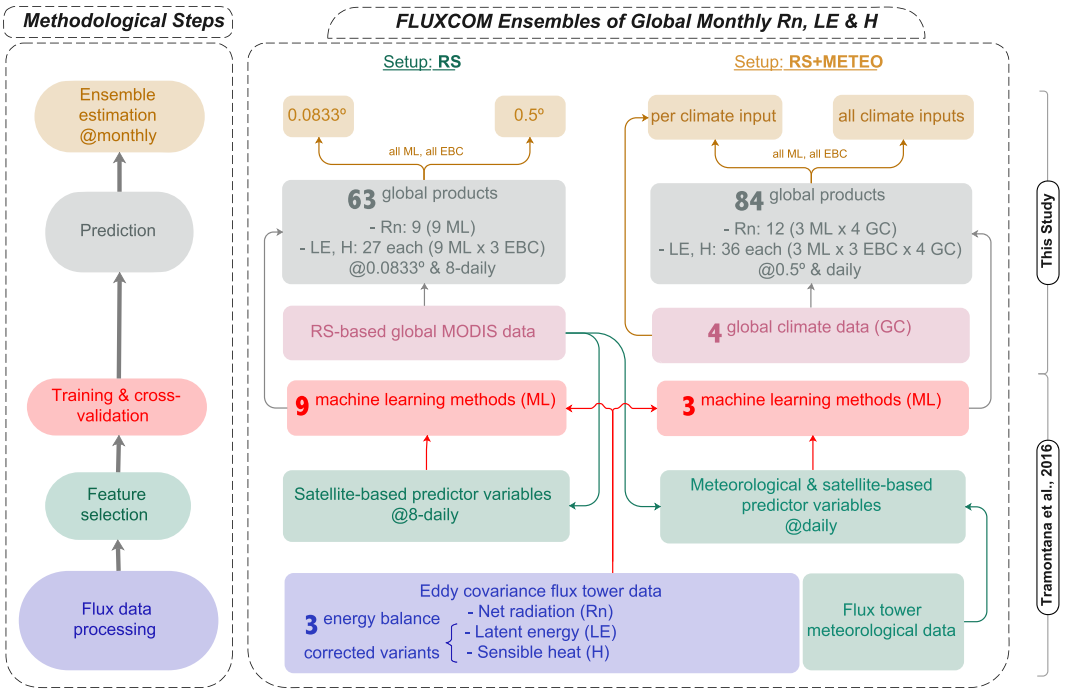

Fig. 1 Schematic overview of the methodology and data products from the FLUXCOM initiative. The flow diagram shows the methodological steps for the remote sensing -based (RS, left) and the remote sensing and meteorological data -based (RS + METEO, right) FLUXCOM products. Final monthly ensemble products for Rn, LE, and H from RS are available at 0.0833° and at 0.5° spatial resolution. Ensemble products from RS + METEO are available per climate forcing data set as well as a pooled ensemble. All ensemble products encompass ensemble members of different machine learning methods (ML, 9 for RS, 3 for RS + METEO) and energy balance corrections (EBC, 3 for LE and H).

meteorological data and mean seasonal cycles of satellite data. Global products of the RS setup have the advantage that they do not require global climate forcing datasets as inputs. Such datasets are themselves subject to uncertainty and are limited in spatial resolution. Not using climate data, however, excludes potentially important information on meteorological conditions for biosphere-atmosphere fluxes and limits temporal coverage to the MODIS era (i.e. 2001 onwards). In contrast, the RS + METEO setup makes use of daily meteorological conditions and through the use of mean seasonal cycles of satellite derived input drivers allows for estimating fluxes beyond the satellite era.

The skill of machine learning-based estimation for both setups at flux tower sites was analysed in detail via cross-validation[22]. The analysis revealed good performance for latent and sensible heat, and in particular for net radiation. Both seasonality and between-site mean fluxes were well predicted, showing more skill than for carbon fluxes (gross primary productivity, terrestrial ecosystem respiration, net ecosystem exchange). Furthermore, only negligible differences were found between different machine learning techniques, and between the RS and RS + METEO setups, which suggests an overall robust extraction of the main patterns of flux variation across methods.

In this study, we used the validated and trained machine learning techniques for the FLUXCOM energy fluxes of Tramontana *et al.*[22] and generated a large ensemble of gridded global flux products (Fig. 1). For the RS setup, nine machine learning methods were used to generate gridded products at an 8-daily temporal and 0.0833° spatial resolution for the 2001–2015 period. For the RS + METEO setup, three machine learning techniques with four global climate forcing data sets yielded products with daily temporal and 0.5° spatial resolution, and time periods (from ~1980 to present) depending on the climate input data. For latent and sensible heat fluxes, we additionally considered uncertainty from a lack of tower-based energy balance closure by propagating three different correction variants. Within the RS and RS + METEO setups, we followed a full factorial design of machine learning methods (9 for RS, 3 for RS + METEO) times energy balance correction variants (3 for LE and H, 1 for Rn), and climate forcing input products (4, only for RS + METEO). To allow for a better reuse of the large archive, we generated ensemble products by pooling machine learning estimates and energy balance closure gap variants. For the RS + METEO setup, this was also done separately for each climate forcing data to allow modellers to compare their simulations with the FLUXCOM ensemble product driven by the same forcing.

Methods

Training of machine learning algorithms. Machine learning methods were trained using observations from 224 flux tower sites following the specifications in Table 1 and detailed previously[22]. Two methods of the RS setup (GPR and RDF-GP) and one for the RS + METEO setup (KRR) which were included in Tramontana *et al.* were not used here due to computational cost. The observed flux tower data had been screened for good quality by

		RS	RS + METEO
Product specifications	Spatial resolution	0.0833°	0.5°
	Temporal resolution	8 daily	daily
	Time period	2001–2015	Depending on climate forcing
	Climate input	n.a.	CRUNCEPv8, WFDEI, GSWP3, CERES-GPCP
	Tiling by PFT	no	yes
	Spatial & Seasonal patterns	f(RS)	f(RS,METEO)
	Interannual & trend patterns	f(RS)	f(METEO)
Training specifications	Machine learning methods	9: RF, ANN, GMDH, MARS, MTE (3 variants), KRR, SVR	3: RF, ANN, MARS
	Number of flux observations for training	~20,000	~200,000
	Spatial features	PFT, Max of MSC(fAPAR*Rg), Min of MSC(Rg)	PFT, Max of MSC(WAI_U), Mean of MSC(BAND 6), Max of MSC(fAPAR*Rg)
	Spatial, seasonal features	Rpot, MSC(EVI*LST_{Day})	Rpot, MSC(NDWI), MSC(LST_{Night}), MSC(EVI*Rg)
	Spatial, seasonal, interannual features	Rg, LST_{Day}, Anom of LST_{Night}, Anom of (EVI*LST_{Day})	Rg, Rain, Rh, Rg*IWA*MSC(NDVI)

Table 1. Specifications of the FLUXCOM RS and RS + METEO setups for energy fluxes. List of acronyms: Enhanced Vegetation Index (EVI), fraction of Absorbed Photosynthetically Active Radiation (fAPAR), daytime Land Surface Temperature (LST_{Day}) and night time Land Surface Temperature (LST_{Night}), Normalized Difference Vegetation Index (NDVI), Normalized Difference Water Index (NDWI), Plant Functional Type (PFT), incoming global Radiation (Rg), top of atmosphere potential Radiation (Rpot), Index of Water Availability (IWA), Relative humidity (Rh), upper Water Availability Index WAI (WAI_U) (for details see Tramontana *et al.*[22] Supplementary Material, Sect. S3), Mean Seasonal Cycle (MSC). Random forest (RF), Artificial Neural Network (ANN), Multivariate Adaptive Regression Splines (MARS), Model-Tree Ensemble (MTE), Kernel Ridge Regression (KRR), and Support Vector Regression (SVR).

(1) allowing for no more than 20% of half-hourly data comprising a daily value to be gap-filled data[23], (2) checking for empirical consistency of energy fluxes, and (3) visual inspection. The same set of valid data points was used for net radiation, latent, and sensible heat flux (i.e. case-wise exclusion). Daily latent and sensible heat fluxes were then corrected for energy balance closure gap at FLUXNET sites using different approaches before training the machine learning algorithms (see below). The choice of satellite based and meteorological predictor variables followed a thorough feature selection analysis using a tailored genetic algorithm[24]. Some predictor variables vary only in space (e.g. plant functional type), some also seasonally (e.g. potential shortwave radiation), and some for each individual time step and location (e.g. short wave radiation, see Table 1). Each machine learning method used the same dataset for training within the RS or RS + METEO setup respectively and used all available data points in contrast to using only 90% of sites as in the cross-validation analysis[22].

Correction for energy balance non-closure at FLUXNET sites prior to training. We used three different approaches to address uncertainty due to the widely observed lack of energy balance closure at FLUXNET sites. The different correction approaches correspond to different hypothesis regarding the primary cause of the energy balance closure gap. The general form of the correction is x_{LE}*LE + x_H*H = Rn-G, where G is the ground heat flux, and x_{LE} and x_H are the correction factors for latent and sensible heat, respectively. The perhaps most widely used approach is the Bowen ratio correction[25] ("BWR", see Table 2), which assumes that the ratio of sensible and latent heat flux is accurately measured, and LE and H are scaled with the same correction factor ($x_{LE\&H} := x_{LE} = x_H$) to force energy balance closure ($x_{LE\&H} = (Rn - G)/(LE + H)$). The "residual approach" ("RES" and "NONE", see Table 2) allocates all missing energy to either LE (LE_{RES} with = x_{LE} = (Rn-G-H)/LE, $x_H = 1$) or H (H_{RES} with x_H = (Rn-G-LE)/H, $x_{LE} = 1$). The correction factors x_{LE} and x_H are estimated as the median of 30 daily values in a moving window. Median values within moving windows were chosen to minimize the impact of noise on x. Very small fluxes (<1 MJ m^{-2} d^{-1}) were not corrected (x = 1) because x can take implausible values when the denominator approaches zero. When G was not measured or missing, it was estimated based on a Random Forest model which was trained on all available daily measurements of G across sites using daily meteorological and energy flux variables as predictors.

Global products of predictor variables for RS products. To produce spatio-temporal grids of energy fluxes, the trained machine learning algorithms require only spatio-temporal grids of input data. We used MODIS land products (collection 5; https://lpdaac.usgs.gov/) as input data for FLUXCOM. The MODIS products include daytime and nighttime land surface temperature (LST; MOD11A2[26]), land cover (MCD12Q1[27]), fraction of absorbed photosynthetically active radiation by a canopy (fPAR) (MOD15A2[28]), and bidirectional reflectance distribution function (BRDF)-corrected reflectances (MCD43B4[29]). Land cover data from 2001 to 2010 were processed to assign the majority land cover class in each 0.0833° grid for the whole period, i.e. land cover change was not considered. The LST, fPAR, and BRDF-corrected reflectances were provided with an 8-daily temporal resolution. The BRDF-corrected reflectances were further converted to vegetation indices: the normalized

Item	Information	Prefix	Values
<EF>	Energy flux	no prefix	-LE, H, Rn
<SETUP>	Upscaling set up	no prefix	-RS: for RS products -RS_METEO: for RS + METEO products
<EBC>	Energy balance correction	EBC-	-ALL: for ensembles that include energy fluxes from all energy balance closure correction methods -NONE: uncorrected energy fluxes -BWR: energy fluxes corrected by Bowen's ratio method -RES: energy fluxes corrected by residual method Note that EBC is always NONE for Rn, because it was never corrected.
<MLM>	Machine learning method	MLM-	-ALL: for ensembles that include energy fluxes from all machine learning methods -ANN, MARS, or RF for energy fluxes from RS + METEO -RF, ANN, MARS, GMDH, KRR, MTE, MTEV, MTEM, or SVM for energy fluxes from RS
<METEO>	Meteorological data	METEO-	-ALL: for RS + METEO ensembles that include energy fluxes from all meteorological data -CERES_GPCP, CRUNCEP_v8, GSWP3, or WFDEI: for RS + METEO products using different meteorological data -NONE: for all energy fluxes from RS (because RS does not use meteorological forcing data)
<sRESO>	Spatial resolution	no prefix	-720_360: for 0.5°x0.5° native RS + METEO and spatially aggregated RS data -4320_2160: for 0.0833°x0.0833° native RS data
<tRESO>	Temporal resolution	no prefix	-monthly: for all data files
<YYYY>	Year	no prefix	-the year for which the data is

Table 2. Key to naming convention used for the folder structure and naming conventions.

difference vegetation index (NDVI), the enhanced vegetation index (EVI)[30], and the normalized difference water index (NDWI)[31].

The processing of the gridded remote sensing data followed the procedure done at flux site-level[22]. Poor quality data were filled to create continuous time-series data. For each time snapshot, bad quality data were identified for each 1 km pixels by the MODIS quality assurance/quality criteria (QA/QC). If more than 25% of 1 km pixels within a 0.0833° grid cell had good quality, the mean of good quality pixels was taken. Otherwise, the value was estimated using the local mean seasonal cycle, i.e. the mean value of other years with accepted quality for the same 8-daily period was used.

For the RS product we used incoming surface shortwave radiation data of the Japan Aerospace eXploration Agency (JAXA) Satellite Monitoring for Environmental Studies (JASMES) product for 2001–2015 period (ftp://suzaku.eorc.jaxa.jp/pub/GLI/glical/Global_05km/repro_v6/). The products are derived from Terra MODIS data with a simple radiative transfer model[32]. The products were previously evaluated for three EC sites in Asia[33] and 20 EC sites in Alaska[34], and showed a good agreement with observations. Spatial and temporal averaging was conducted by converting the original 5 km grid to 0.0833° grids and daily to 8-daily temporal resolution. Missing data in the original 5 km data were replaced by mean daily values of available years.

Global products of predictor variables for RS + METEO products. Mean seasonal and mean annual characteristics of MODIS-based remotely sensed land surface variables (see Table 1 and Tramontana *et al.* for details) were tiled by plant functional type, i.e. grids for each PFT containing the mean value per PFT and time step at 0.5° were created. Mean seasonal cycles of daily MODIS data for each grid cell used in the RS + METEO setup were computed by linearly interpolating a temporally smoothed mean seasonal cycle of 8-daily values. The land cover fractions are based on the same product and approach as in the RS product.

For daily meteorological variables four different commonly used global climate forcing data sets were chosen: WATCH Forcing Data ERA Interim (WFDEI[35], 1979–2013, ftp://rfdata:forceDATA@ftp.iiasa.ac.at), Global Soil Wetness Project 3 forcing (GSWP3[36], 1950–2014,), CRUNCEPv8[37] (1950–2016, https://vesg.ipsl.upmc.fr/thredds/catalog/work/p529viov/cruncep/V8_1901_2016/catalog.html), and a combination of radiation based on CERES[38] and precipitation from GPCP[39] (CERES-GPCP, 2001–2014, https://ceres.larc.nasa.gov/, https://precip.gsfc.nasa.gov/). The water availability index and the index of water availability, (WAI and IWA, see supplement 3 in Tramontana *et al.*[22]), were calculated for each forcing data set based on daily precipitation and potential evapotranspiration. The native spatial resolution of all four climate forcing datasets was 0.5° except for CERES-GPCP (1°). Here, CERES based radiation and GPCP based precipitation data were regridded to 0.5° by splitting up the original 1° grid cells into 0.5° grid cells.

Generation of global products (Prediction). For the RS products, the trained machine learning models were applied to the gridded predictor variable fields for each 8-daily time step with a spatial resolution of 0.0833°. For the RS + METEO products, the trained machine learning models were run for each daily time step and for each plant functional type (PFT) at a 0.5° spatial resolution separately, and a weighted mean over the PFT fractions was obtained for each gridcell and time step. Note that the fraction of unvegetated (barren, permanent snow or ice, water) area was omitted in that calculation such that the definition of the calculated flux densities are per vegetated area (rather than grid cell or land area). The omission of deserts was necessary due to a lack of flux tower data. This complicates the assessment of globally integrated fluxes for sensible heat and net radiation where these fluxes typically show large positive and negative fluxes for hot and cold deserts, respectively. All computations were performed with MATLAB on a high-performance computing cluster at the Max Planck Institute for Biogeochemistry, Jena.

Spatial and temporal aggregation of FLUXCOM-RS products. To facilitate broader reuse of the FLUXCOM-RS products originally at 0.0833° and 8-daily time step we derived monthly products at 0.0833° and 0.5°. The monthly temporal aggregation is based on linearly interpolating the 8-daily data into daily data followed

by calculating monthly averages. The spatial aggregation to 0.5° is based on taking the mean value of non-missing data points within each 0.5° cell.

Ensemble estimates. For the RS setup, we generate ensemble products at 0.0833° and 0.5° spatial resolution for each flux (LE, H, Rn) by pooling all the different runs per machine learning method (9) and energy balance correction variants (3, only for LE and H). This yields 27 ensemble members for LE and H, and 9 for Rn for the RS ensembles.

For the RS + METEO setup, we generated ensembles for each climate forcing data by pooling the runs for three machine learning methods and energy balance correction variants (3, only for LE and H). For each climate forcing specific ensemble, this yields 9 ensemble members for LE and H, and 3 ensemble members for Rn. We additionally generated an overall RS + METEO ensemble by pooling runs for different climate forcing data, machine learning methods, and energy balance correction variants. For the overall RS + METEO ensemble this yields 36 ensemble members for LE and H, and 12 for Rn.

The ensemble products were generated for mean monthly fluxes where the ensemble estimate is the median over ensemble members for each gridcell and month. In addition, we included the median absolute deviation as a robust estimate of ensemble spread, i.e., uncertainty. For the RS ensemble, the ensemble spread captures uncertainty related to the choice of machine learning method and the lack of energy balance closure seen in FLUXNET data. For the overall RS + METEO ensemble, the ensemble spread captures uncertainty related to the choice of machine learning method, the energy balance closure gap issue, and the choice of climate forcing data. Due to space restrictions and conciseness, results and technical validation (see below) focus on a parallel assessment of the RS and the RS + METEO ensemble. Occasionally we make use of all ensemble members where appropriate (see Figure captions).

Cross-consistency checks with the state-of-the-art estimates. We compare the spatial patterns of mean annual LE and Rn fluxes as well as monthly time series of their continental means from the FLUXCOM ensemble against previous estimates. For LE, we compare FLUXCOM RS and RS + METEO ensembles against those from Model Tree Ensemble (MTE[10]), the Global Land Evaporation Amsterdam Model (GLEAM v3.1a[40]), and LandFlux-EVAL[41]. The MTE is based on only one machine learning method[8] trained on monthly flux data[9,10] and may be regarded as a precursor to FLUXCOM. GLEAM (https://www.gleam.eu/) models evapotranspiration based on a Priestley-Taylor formulation[42] with explicit soil moisture stress, and the interception by the Gash model[43], and was informed by various satellite forcing data. LandFlux-EVAL (http://www.iac.ethz.ch/group/land-climate-dynamics/research/landflux-eval.html) is the ensemble mean of 14 evapotranspiration products of different approaches. For the conversion between evapotranspiration and latent heat we assumed a constant latent heat of vaporization of 2.45 MJ mm^{-1}.

For Rn, we compare against two satellite-based products from Clouds and the Earth's Radiant Energy System (CERES, https://ceres.larc.nasa.gov/) SYN1d Ed4A product[38] and Surface Radiation Budget (SRB, https://eosweb.larc.nasa.gov/project/srb/srb_table) release 3.1. Both products combine diverse atmospheric satellite data extensively with data assimilation, while SRB can be regarded as a precursor to CERES. For comparison with FLUXCOM, the original 3-hourly data were aggregated to monthly means and resampled from 1° to 0.5° using the nearest neighbour method. In the RS + METEO setup, the CERES shortwave radiation was used as an input for one meteorological forcing variant (CERES-GPCP), i.e., for one fourth of the ensemble members of RS + METEO. Thus, the produced net radiation of the FLUXCOM RS + METEO ensemble is not fully independent from the net radiation of CERES. However, the RS product did not use CERES data and is therefore independent.

The comparisons of all data products use the common 2001–2005 period and a common mask for vegetated land area. Differences in masking may lead to some differences in mean global numbers compared to those reported elsewhere. We compare mean annual fluxes across space and provide Pearson's correlation coefficient, equations of a linear total least squares fit, and density scatter plots of mean annual fluxes using gridcells with a land fraction of at least 80% to minimize inconsistencies in cross-product comparisons. For continental mean monthly fluxes, we calculated the mean and median absolute deviation (MAD) across all ensemble members for each monthly time step. MAD was converted into a robust estimate of 1 standard deviation by multiplying it with 1.4826 (assuming a normal distribution[44]). The calculation of global and continental mean annual energy fluxes and their uncertainty also follows the procedure of first aggregating each ensemble member for the period 2001–2013, but the common mask of valid data from the intersection with independent products was not used.

For an unbiased comparison of FLUXCOM sensible heat and net radiation fluxes with global values from the literature, we scaled FLUXCOM products to incorporate fluxes from non-vegetated area of the world. The non-vegetated land area not covered by FLUXCOM products corresponds to cold (mainly Greenland and Antarctica) and hot (mainly Sahara) deserts. For hot deserts, we estimated a mean sensible heat flux based on CERES net radiation and GPCP precipitation assuming that all precipitation is converted to latent heat and subtracted from Rn. The average values were computed for grid cells where the fraction of hot desert exceeds 50% and resulted: 5.9356 MJ m^{-2} day^{-1} for Rn and 5.8264 MJ m^{-2} day^{-1} for H for the period 2001–2010. For cold deserts we obtained mean Rn as −0.1826 MJ m^{-2} day^{-1} from CERES, while H was derived by a previously calculated value[45] of −33.2 W m^{-2} (−2.8685 MJ m^{-2} day^{-1}) based on reanalysis. The global adjusted value of FLUXCOM for sensible heat or net radiation was then computed as a weighted average for the three area fractions: vegetated = 0.765, cold deserts = 0.108, hot deserts = 0.1265, where the vegetated value is directly from FLUXCOM.

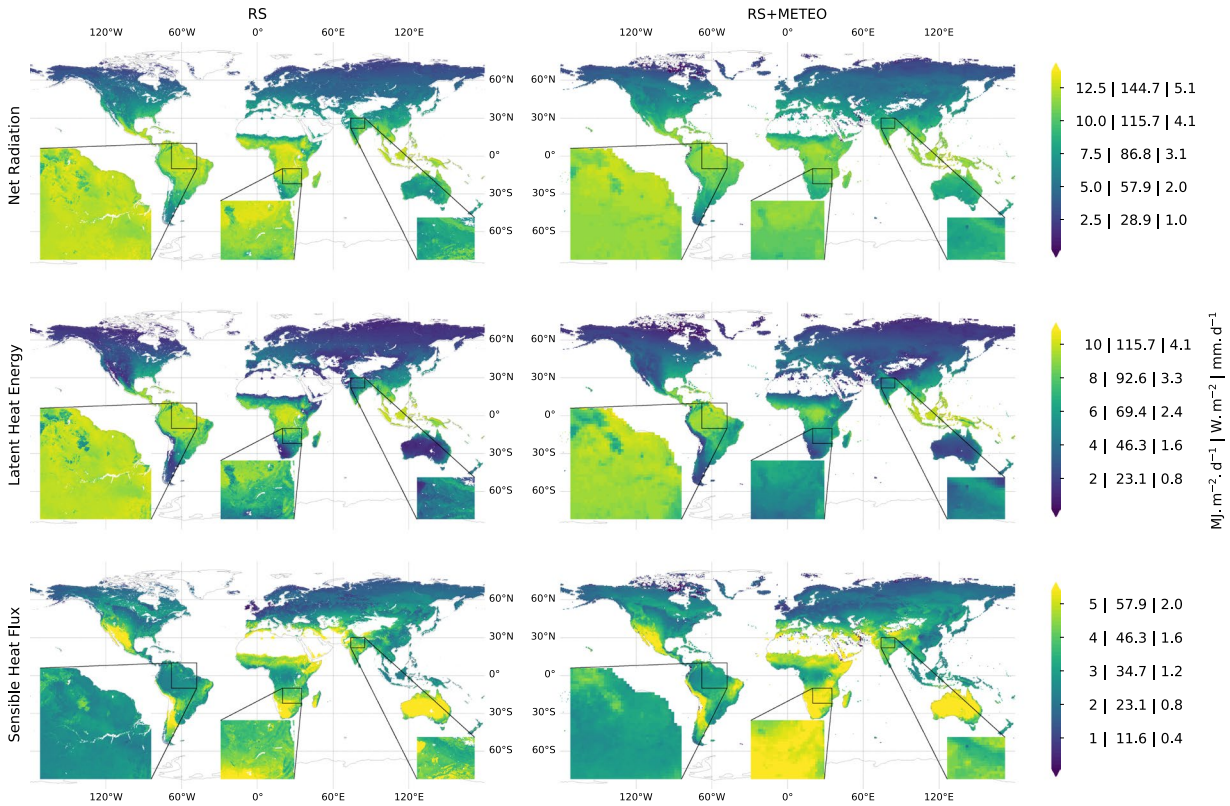

Fig. 2 Global distributions of mean annual (2001–2013) energy fluxes from the FLUXCOM RS and RS + METEO ensembles. The fluxes are expressed in $MJ\ m^{-2}\ d^{-1}$, $W\ m^{-2}$, and $mm\ d^{-1}$, separated by '|', in the color bars. Inset figures show zooms for different regions.

Data Records

The native FLUXCOM energy flux products amount to more than 4 TB of data. Products with daily or 8-daily temporal resolution or customized ensemble estimates are available on request to Martin Jung (mjung@bgc-jena.mpg.de). Monthly energy flux data of all ensemble members as well as the ensemble estimates from the FLUXCOM initiative (http://www.fluxcom.org) described here[46] are freely available (CC4.0 BY licence) from the data portal of Max Planck Institute for Biogeochemistry after registration. Choose 'FluxCom' in the dropdown menu of the database and select FileID 257. The users will be provided with an access to a ftp server. The ftp directory stores 214 GB of data and is structured in a consistent way with the file naming in Table 2. The folder structure was designed to facilitate easy download of relevant subsets of the archive and is as per the following convention:

<SETUP>/<TYPE>/<sRESO>/<tRESO> or <SETUP>/<TYPE>/<METEO>/<tRESO>

<SETUP> is either "RS" or "RS_METEO". <TYPE> is either "ensemble" or "member". At the third level, RS uses <sRESO> ("720_360" for 0.5° or "4320_2160" for 0.0833° resolution) and RS + METEO uses <METEO> (see Table 2). <tRESO> is always "monthly" for the currently available data in the portal. For the data at other temporal resolutions, which are available upon request, tRESO can also be daily, 8 daily, or annual.

The files are provided in network Common Data Form, version 4 (netCDF-4) data format (https://www.unidata.ucar.edu/software/netcdf/). The data files are named using the following convention:

<EF>.<SETUP>.<EBC>.<MLM>.<METEO>.<sRESO>.<tRESO>.<YYYY>.nc

The details of each of the <item> in the filenames are provided in Table 2.

For example, the file "LE.RS.EBC-ALL.MLM-ALL.METEO-NONE.720_360.monthly.2001.nc" is the RS-based ensemble latent heat energy of year 2001 that includes all fluxes produced using all energy balance closure correction methods and all machine learning methods and no meteorological data aggregated to 0.5° spatial resolution (size 720 along longitude and 360 along latitude) and monthly temporal resolution.

For all types (ensemble or member) of data, the variable names for latent heat energy, sensible heat, and net radiation are LE, H and Rn, respectively. The data files for both RS and RS + METEO -based ensembles include additional variables with suffix '_MAD' (e.g., LE_MAD). This variable provides the data for uncertainty (median absolute deviation) among different ensemble members for each grid cell and month. The '_MAD' uncertainty variable is also in the same time, latitude, longitude coordinates. The ensembles from RS + METEO products, that include runs with four different forcing inputs, also have a variable with '_n' (e.g., LE_n in latitude, longitude coordinates). This variable stores the number of ensemble members included while calculating the median. The

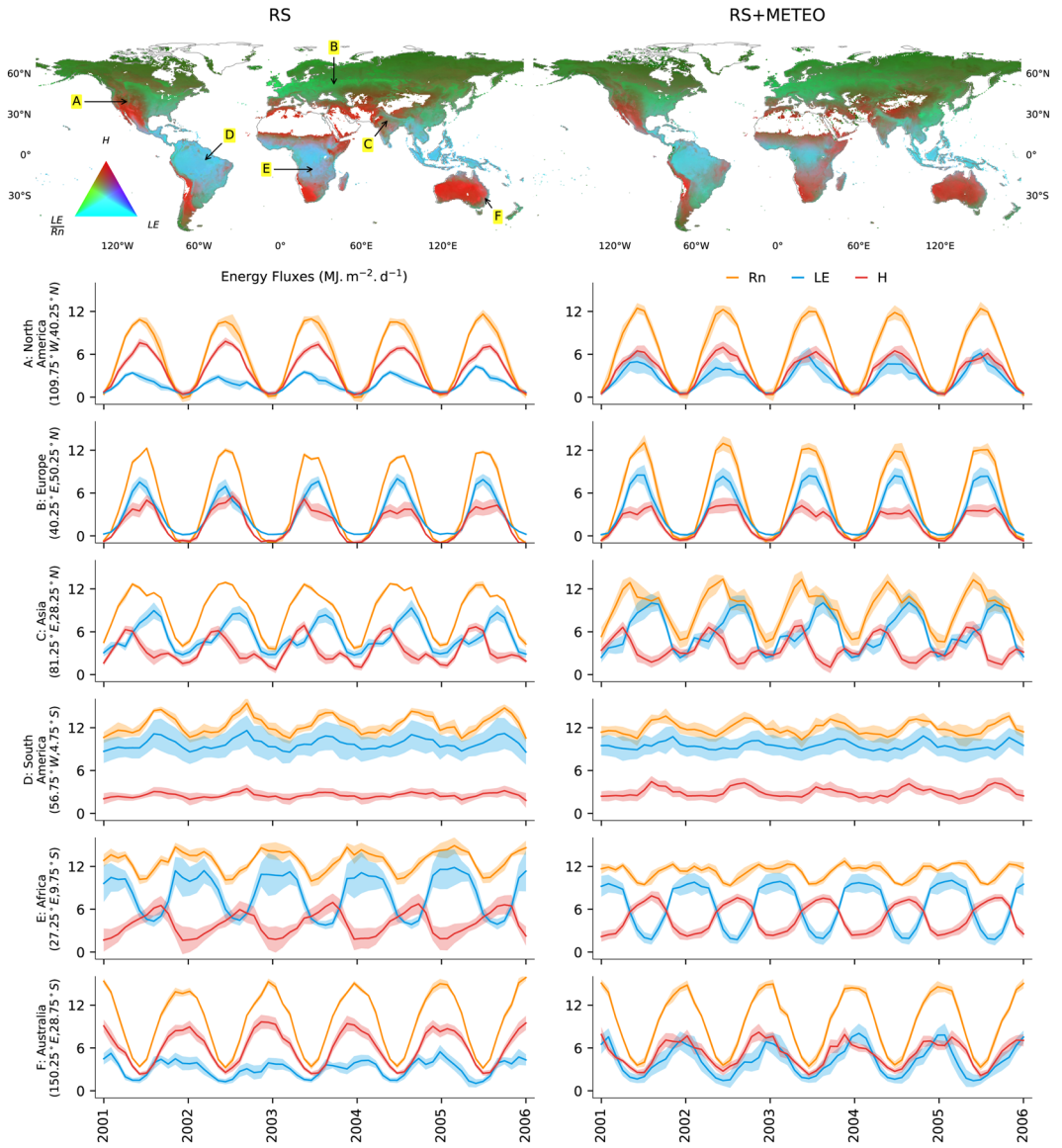

Fig. 3 Global covariations of land-atmosphere energy fluxes, and their temporal variations and uncertainties in selected locations. RGB composite maps are with latent heat (*LE*) in the blue, sensible heat flux (*H*) in the red, and evaporative fraction (LE/Rn) in the green channel. Line plots show time series of *LE* (blue), *H* (red), and *Rn* (orange) for selected locations (0.5° grid cells, see map for RS) from 2001 to 2005 in $MJ\ m^{-2}\ d^{-1}$. The shades around the lines indicate the uncertainty ranges (±1 robust standard deviation) of ensemble members.

number of ensemble members varies in space in RS + METEO ensembles, because of the difference in land-sea mask of different meteorological data used. The data for each variable is defined by 3 dimensions: 'lat' for latitudes and 'lon' for longitudes in space, and 'time' for time. The data variables are defined by time, latitude, longitude coordinates. The header of the netCDF-4 data files includes the global attributes that lists the product (RS + METEO or RS), type of the data (either member or ensemble), the machine learning method(s), and meteorological data used (as per Table 2).

Additionally, we have included ancillary data (in a directory named "ancillary") for land and vegetated area fraction per grid cell. The files are named using "<variable name>.<sReso>.nc" convention. The <variable name> is "landfraction" for the fraction of land within a grid cell, and "vegfraction" for the fraction of the land fraction that has vegetation cover. The <sReso> reflects the spatial resolution, and is "720_360" for fractions corresponding to 0.5° products, or "4320_2160" those corresponding to 0.0833° RS products.

Technical Validation

In this section, we present the main spatiotemporal features of the FLUXCOM energy fluxes. We validate patterns and magnitudes of fluxes against previous state-of-the-art estimates, and expectations from theory and literature.

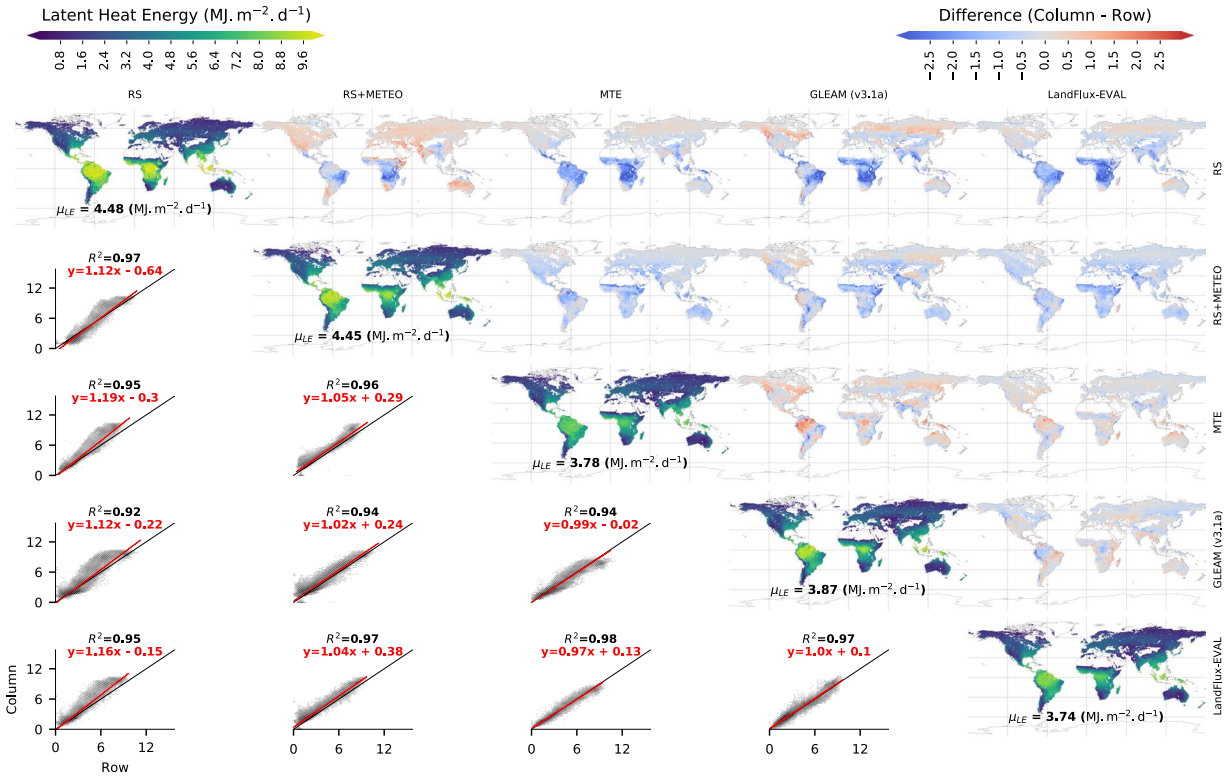

Fig. 4 Comparison of the global distributions of mean latent heat (LE) fluxes from FLUXCOM against previous global estimates. Along the diagonal, maps of means for the period 2001–2005 from RS + METEO, RS, MTE, GLEAM v 3.1a, and LandFlux-EVAL are plotted along with the area weighted mean LE (μ_{LE}) as text. Above the diagonal, the difference maps for each of these products (column - row) are plotted. Below the diagonal, density scatter plots between these products are provided with darker shade indicating larger density of points. Here, black lines show the 1:1 line, red lines show the total (orthogonal) least square regression fit with the equation given in red text and the coefficient of determination (squared Pearson's correlation coefficient, R^2).

Consistent with current understanding, mean annual latent heat and net radiation fluxes are the highest in tropical and the lowest in high latitude regions of the world (Fig. 2). In contrast, mean annual sensible heat peaks in dry sub-tropical regions where latent heat fluxes are reduced due to expected water limitation on evapotranspiration which is known to increase the Bowen ratio (H/LE). These patterns are qualitatively consistent among the RS and RS + METEO ensemble products, while flux magnitude differences, e.g., larger net radiation of the RS product in the tropics, are also evident. In general, both RS and RS + METEO products show similar large-scale variations in energy fluxes but local-scale heterogeneities are better resolved in RS products (see the inset zoom-ins in Fig. 2) due to a 6-fold increase in spatial resolution.

The maps of Fig. 3 provide a visual impression of the global spatial co-variation of energy fluxes. In these RGB maps, hot and dry regions appear as red where latent heat is low and net radiation is preferentially converted to sensible heat. Wet tropical regions with high net radiation and latent heat but low sensible heat appear as cyan. Regions where latent heat is energy-limited but net radiation is intermediate or low appear in green. The partitioning of Rn into LE and H components is similar for both RS + METEO and RS products (Fig. 3) with some regional differences visible. To illustrate local differences among the RS and RS + METEO ensemble products, as well as seasonal variations of energy fluxes and its uncertainties, we present time series of selected locations (0.5° grid cells) in Fig. 3. For example, in the selected location in North America (A), situated at the transition between water limited and energy limited regime of evapotranspiration, we see more H relative to LE in the RS ensemble compared to the RS + METEO ensemble. Similar patterns of slightly different net radiation partitioning in LE and H are also evident in other transitional locations in Africa (E) and Australia (F). Energy flux uncertainties (see shading in Fig. 3) vary spatially, seasonally, and interannually as well as between the RS and the RS + METEO ensemble products. Where uncertainties of the RS + METEO ensemble are larger compared to the RS ensemble, it suggests larger contributions of meteorological forcing data uncertainty. On the other hand, larger uncertainty of the RS ensemble may indicate larger contribution of machine learning method choice, perhaps due to poor constraints by flux tower stations. Overall, there is high level of consistency between the RS and RS + METEO ensemble products for seasonality and flux magnitudes as well as their uncertainties.

We further evaluate the spatial patterns of mean annual energy fluxes of the FLUXCOM ensemble against previous estimates. First, we evaluate the long-term mean LE from RS and RS + METEO against those from MTE[10], GLEAM v 3.1a[40], and LandFlux-EVAL[41]. Generally, the spatial variation of ET is very consistent between FLUXCOM products and previous global estimates (Fig. 4) with R^2 values close to 1. All show the dominant

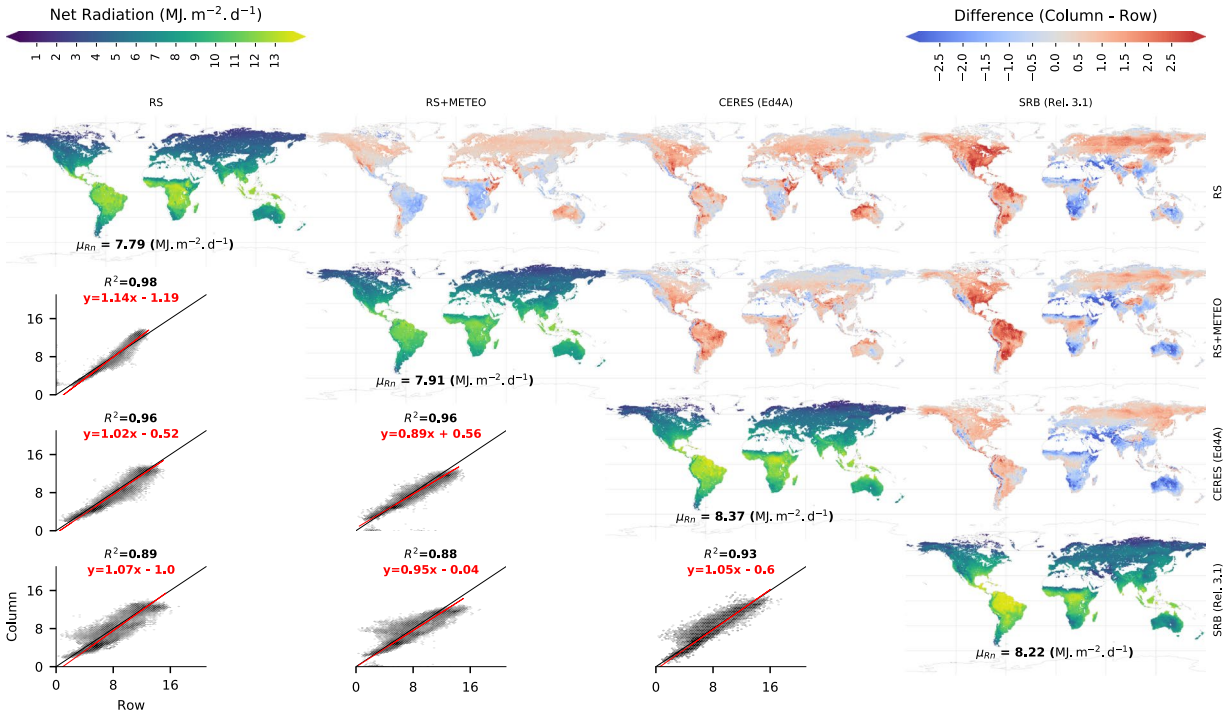

Fig. 5 Comparison of the global distributions of mean net radiation (Rn) from FLUXCOM against previous global estimates. Along the diagonal, maps of the means for the period 2001–2005 from RS + METEO, RS, CERES, and SRB are plotted. See Fig. 4 for further explanations. Note that the color scale of the difference maps is the same as for the LE (Fig. 4) despite the larger flux magnitudes of Rn.

gradient between the highest LE in the humid tropics and the lowest LE in cold and dry places. There are however sizeable systematic differences between products, in particular within the tropics. Both RS and RS + METEO show larger LE in the tropics than MTE and LandFlux-EVAL while GLEAM shows regionally similar LE magnitudes in the wet tropics. The larger tropical LE in FLUXCOM propagates to 15–20% larger global means of LE compared to the other two estimates (see below for a broader comparison of global LE estimates). Due to the large LE flux in the wet tropics, even a comparatively small relative difference results in large absolute differences. In the tropical regions, the difference between RS and RS + METEO LE is also relatively large with larger LE in RS. But, globally, this difference is somewhat balanced by lower LE in RS in other regions. Semi-arid regions also tend to show comparatively large systematic differences across products.

For Rn, we compare the spatial patterns of FLUXCOM products against two satellite-based products from CERES[38] and SRB. The spatial patterns of mean annual Rn from RS and RS + METEO agree better with CERES ($R^2 = 0.96$) than the agreement between CERES and SRB ($R^2 = 0.93$) (Fig. 5). The RS product and CERES show larger Rn in the tropics compared to RS + METEO. Large differences between SRB and all other products are evident both in tropical and extratropical regions, South America, large parts of North America and across Eurasia. CERES as well as SRB tend to show larger Rn in many extratropical regions compared to both FLUXCOM ensemble products. This contributes to a 4–7% larger global vegetated Rn of CERES and SRB compared to FLUXCOM products.

We further compare the monthly variations of global and continental-scale energy fluxes (Fig. 6) against previous estimates. There is a very high agreement among all with respect to seasonality. In all continents except Africa, the previous estimates are within the 1 standard deviation of RS and RS + METEO FLUXCOM products. In Africa, LE is higher in FLUXCOM products, which contributes to the slightly larger global ET in FLUXCOM than previous estimates. For Rn, the differences are relatively smaller in all continents and uncertainties obtained from the FLUXCOM ensemble are small compared to those of LE and H. The uncertainty estimates of LE in both RS and RS + METEO energy fluxes show distinct seasonal variation in all continents. In Africa and South America, the uncertainty ranges are larger in all seasons. In other continents, the uncertainty ranges are larger in the peak season and generally scale with flux magnitude.

We have further summarized mean annual energy budgets with uncertainties for the vegetated area of the globe and over all continents (Fig. 7a). The global and continental energy budgets of the RS and RS + METEO products are consistent with each other. Globally, both RS and RS + METEO products show that most of Rn is partitioned to LE. Only Oceania (dominated by Australia) shows more sensible than latent heat. In Africa, LE is significantly larger than H due to the exclusion of the non-vegetated Sahara Desert, where H is expected to be much larger than LE.

The mean annual imbalance of the ensemble medians, defined as Rn-LE-H is close to zero. This indicates that the tower-to-globe scaling across all energy balance correction variants is robust and did not introduce sizeable

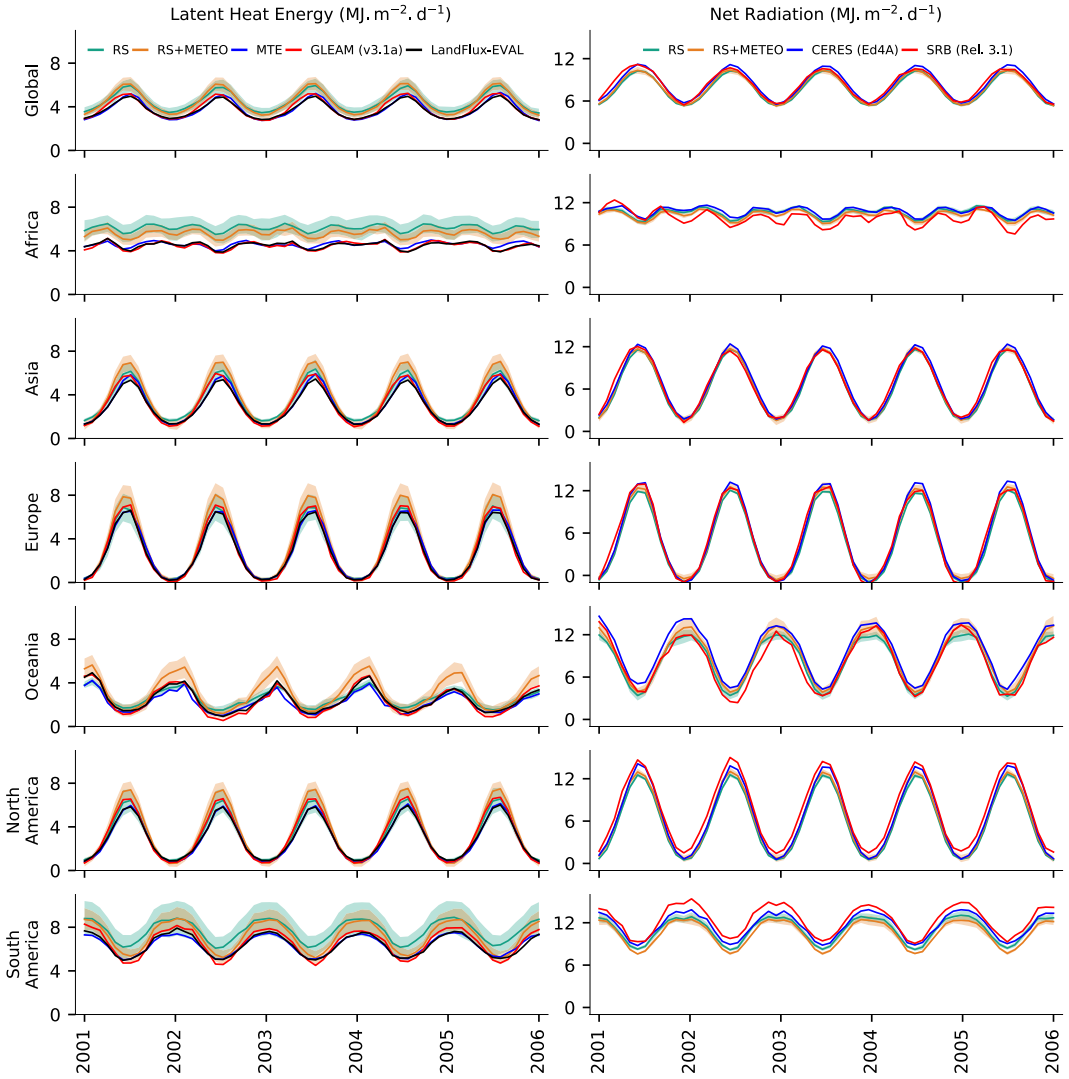

Fig. 6 Comparison of the temporal variations of global and continental latent heat energy (LE) and net radiation fluxes (Rn) from FLUXCOM with previous estimates. The shaded region across the RS + METEO and RS lines indicate the uncertainty (±1 robust standard deviation) of ensemble members. Note the different axes limits for LE and Rn.

biases. Inspecting relative uncertainties of the mean global and continental fluxes (Fig. 7b), we find that Rn is typically constrained by less than 5%, uncertainties for latent and sensible heat fluxes are typically on the order of 10–20%. The contributions of the different factors (energy balance correction, machine learning method, and meteorological forcing) to the total ensemble spread varies by flux and continent (Supplementary Information 1).

For comparisons with published global estimates, we scaled FLUXCOM values using estimates of H and Rn for hot and cold deserts (see Methods). We obtained mean global values of H of 2.80 ± 0.36 MJ m^{-2} day^{-1} for the RS products and 3.07 ± 0.41 MJ m^{-2} day^{-1} for the RS + METEO products, or, equivalently, 32.39 ± 4.17 and 35.58 ± 4.75 W m^{-2} (uncertainties taken from Fig. 7a) respectively. These values are larger than the 27 W m^{-2} reported by Trenberth *et al.*[47] and somewhat smaller than the range of 36–40 W m^{-2} given by Siemann *et al.*[45]. FLUXCOM estimates are however in good agreement with the values of Wild *et al.*[4] of 32 W m^{-2} as a best estimate derived as energy budget residual of observational data and the value of 38 ± 6 W m^{-2} estimated by L'Ecuyer *et al.*[3] based on constraining the global energy and water cycles by multiple data streams. Scaled FLUXCOM Rn (see Methods) yields 75.49 ± 1.39 W m^{-2} and 77.52 ± 2.43 W m^{-2} for RS and RS + METEO, respectively, which is in excellent agreement with the best estimate of L'Ecuyer *et al.*[3] of 76 W m^{-2}.

Because latent heat, as evapotranspiration (ET), is also a critical component of the water cycle, we summarize the continental and global ET from FLUXCOM (Fig. 8). Globally, the ET from RS and RS + METEO are 75.6 ± 9.8 and $76 \pm 6.8 \times 10^3$ km^3 yr^{-1}, respectively. These global ET are at the upper end of previously reported values (65–75 $\times 10^3$ km^3 yr^{-1}). Several studies[9,48–50] indicated global ET in the range of 65 to 70 $\times 10^3$ km^3 yr^{-1}. More recently, global ET values in the range of 70–75 $\times 10^3$ km^3 yr^{-1} were reported[51–53]. Interestingly, global ET estimated from an energy balance perspective also tend to yield values at the upper end of commonly reported

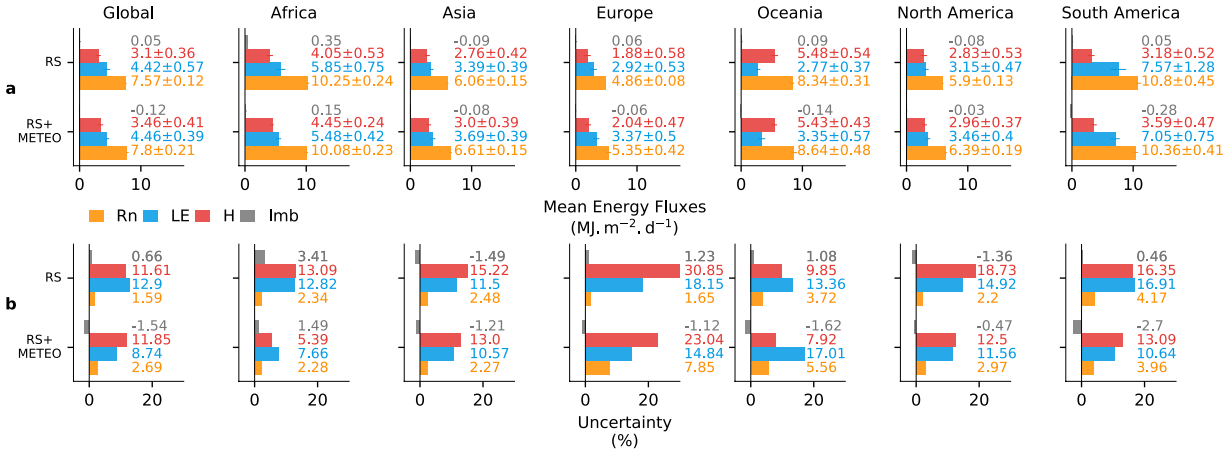

Fig. 7 Overview of the global and continental estimates of energy fluxes from FLUXCOM with uncertainties. (**a**) Bars represent ensemble median of long-term means (2001–2013) of ensemble members for net radiation (Rn, orange), latent heat (LE, blue), sensible heat (H, red), and the energy imbalance of the ensemble medians (Imb, Rn-LE-H, grey) and error bars refer to one robust standard deviation (not available for Imb). (**b**) Bars represent uncertainties relative to the ensemble median in %; the relative uncertainty of Imb is (Rn-LE-H)/Rn. Note that all estimates refer to the respective vegetated area.

values such as Trenberth[47] (73×10^3 km^3 yr^{-1}), L'Ecuyer[3] ($72 \pm 5 \times 10^3$ km^3 yr^{-1}), and Wild[4] (72 within a range of 64–85 $\times 10^3$ km^3 yr^{-1}).

Around three quarters of the global ET is equally distributed across Africa (23.2–25.5%), Asia (25.9–28.1%) and South America (23.7–26.1%), while the lowest contribution is from Oceania (4.4–5.1%), in both RS and RS + METEO (Fig. 8a). Both RS and RS + METEO show sizeable uncertainty ranges of global and continental ET (Fig. 8b). In all continents, the ensemble medians of RS and RS + METEO overlap. In Asia, Europe, Oceania, and North America, RS + METEO has larger uncertainties than RS, while the opposite is true in Africa and South America.

Usage Notes

For cross-consistency analysis and evaluation of LSM simulations, we suggest focusing on spatial patterns of mean annual and mean seasonal fluxes. For comparison with offline LSM simulations we recommend using products from the RS + METEO setup forced with corresponding meteorological forcing to minimize deviations due to different climate input data. However, as RS + METEO inputs prescribe seasonal and spatial land surface properties–through mean seasonal cycles and PFT-based tiling respectively–full consistency with forcing-specific LSM simulations cannot be achieved. For example, while fAPAR is prescribed by remote sensing covariates in FLUXCOM, it may be simulated by the LSM from the climate forcing. Since products from the RS setup are not subject to uncertain meteorological inputs, the RS products may be preferable for energy and water budget studies or for evaluating the choice of climate input driver on LSM simulations.

Patterns of interannual variations in these products are expected to be more uncertain than spatial patterns of mean annual or seasonal fluxes. Experiences from FLUXCOM carbon fluxes suggest that magnitudes of interannual variations[54] are also likely too small in the energy flux products, and a normalization of the monthly or annual anomalies is recommended when comparing for example with LSM simulations. For example, global grids of LSM and FLUXCOM anomalies could be normalized by their standard deviations of the globally integrated anomaly time series to preserve spatiotemporal patterns but to remove differences in variance. Note that interannual variations in the RS + METEO products originate exclusively from direct effects of changing meteorological forcing with remotely sensed surface properties being constant between years. This is particularly important for studies on phenology or the impact of land surface changes on land-atmosphere energy fluxes, where we would recommend using RS setup products. Low frequency variations and trends require very cautious interpretation as factors expected to cause trends, most importantly the physiological effects of rising CO_2, are not accounted for. Trends in land surface properties such as greening or browning are not accounted for in the RS + METEO setup since mean seasonal cycles of MODIS land products were used here. In comparison, the RS products do have these trends included, but due to issues with sensor age-based drift in MODIS reflectances, caution is warranted.

The energy flux densities of FLUXCOM product are defined per vegetated area in each grid cell. This needs to be considered when calculating global and continental budgets, in particular for sensible heat and net radiation where these fluxes have sizeable magnitudes over non-vegetated areas (see Technical validation). The land fraction provided with the FLUXCOM data should be multiplied with the flux densities for a correct accounting of fluxes over land. Please note that FLUXCOM data should not additionally be multiplied with grid cell specific vegetated area fraction as we assume that varying vegetation cover is implicit in the used remote sensing data. The primary intended use of the provided vegetated area fraction data is for comparisons with LSM outputs, e.g. to ensure that the comparison includes only grid cells with (nearly) full vegetation cover in FLUXCOM and LSM simulations.

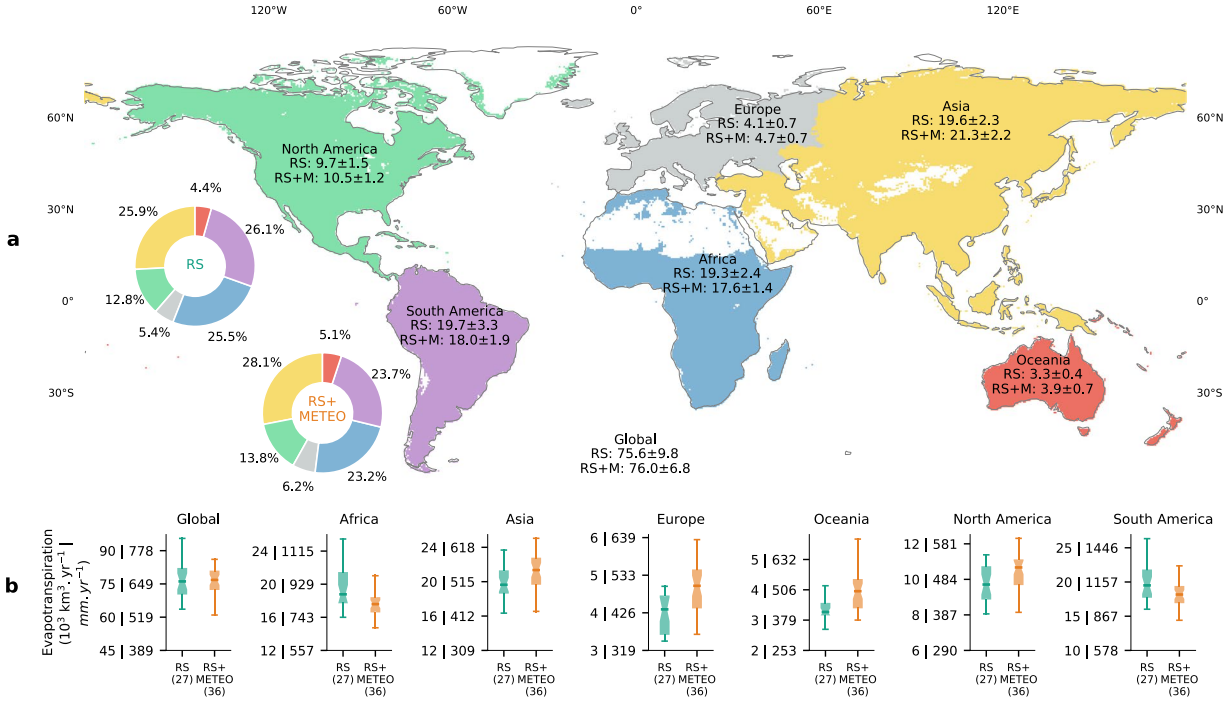

Fig. 8 Overview of the global and continental evapotranspiration (*ET*) fluxes from FLUXCOM. (**a**) Continental estimates of the ensemble median ± 1 robust standard deviation of RS and RS + METEO (RS + M) ensemble members in *1,000* km^3 yr^{-1}. Donut charts show the relative contributions of each continent to the global *ET* with colours corresponding to the map. (**b**) Box plots show the ensemble spread of the 27 and 36 members for RS and RS + METEO respectively, where the whiskers indicate the 1.5 times interquartile range. Note that the y-axis scale changes between continents, and that labels for ET in *mm* yr^{-1} are with respect to the vegetated area.

When using FLUXCOM ensemble members to address questions related to the energy balance and its uncertainty, it must be considered that only certain combinations of energy balance corrected latent and sensible heat fluxes correspond to energy balance closure: i) LE_{NONE} and H_{RES}, ii) LE_{RES} and H_{NONE}, and iii) LE_{BWR} and H_{BWR}. All other combinations result in under or over-closure of the energy balance and should not be considered. The ensemble products presented here pool over all energy balance correction variants such that the energy balance is closed from a conceptual point of view. Remaining closure errors originate from upscaling errors from site to globe.

FLUXCOM ensemble products provide the median absolute deviation of ensemble members per grid cell and time step which might be scaled to a robust estimate of the standard deviation of a normal distribution by multiplying with 1.4826. A propagation of this spatially and temporally explicit uncertainty to a temporal aggregated (e.g. mean annual) or spatial (e.g. continental) uncertainty would require assumptions on error co-variances in space and time. In such cases, we recommend to perform the desired aggregation for each ensemble member separately and subsequently take the spread of the aggregated ensemble members as the uncertainty metric. If users require a different combination of ensemble members other than those presented here, have questions or want to give feedback, please contact Martin Jung (mjung@bgc-jena.mpg.de).

Code Availability

Python code to synthesise the results and to generate the figures of FLUXCOM results can be obtained through the public repository at https://git.bgc-jena.mpg.de/skoirala/fluxcom_ef_figures. MATLAB code for generating the flux products and ensemble estimates is available on request to Martin Jung (mjung@bgc-jena.mpg.de) for the sake of reproducibility. The collaborative nature of the FLUXCOM initiative and the demanding computing resulted in complex and large amounts of code that was customized to the HPC and file system of MPI-BGC and is therefore challenging to use. Code for processing MODIS satellite data is available on request to Kazuhito Ichii (ichii@chiba-u.jp).

References

1. Jimenez, C. *et al.* Global intercomparison of 12 land surface heat flux estimates. *Journal of Geophysical Research - Atmospheres* **116**, D02102 (2011).
2. Mueller, B. *et al.* Benchmarnk products for land evapotranspiration: LandFlux-EVAL multi-data set synthesis. *Hydrology and Earth System Sciences* **17**, 3707–3720 (2013).
3. L'Ecuyer, T. S. *et al.* The Observed State of the Energy Budget in the Early Twenty-First Century. *Journal of Climate* **28**, 8319–8346 (2015).

4. Wild, M. *et al*. The energy balance over land and oceans: an assessment based on direct observations and CMIP5 climate models. *Climate Dynamics* **44**, 3393–3429 (2014).
5. Zhang, Y. *et al*. A Climate Data Record (CDR) for the global terrestrial water budget: 1984–2010. *Hydrology and Earth System Sciences* **22**, 241–263 (2018).
6. Baldocchi, D. TURNER REVIEW No 15. 'Breathing' of the terrestrial biosphere: lessons learned from a global network of carbon dioxide flux measurement systems. *Australian Journal of Botany* **56**, 1–26 (2008).
7. Stoy, P. C. *et al*. A data-driven analysis of energy balance closure across FLUXNET research sites: The role of landscape scale heterogeneity. *Agricultural and Forest Meteorology* **171–172**, 137–152 (2013).
8. Jung, M., Reichstein, M. & Bondeau, A. Towards global empirical upscaling of FLUXNET eddy covariance observations: validation of a model tree ensemble approach using a biosphere model. *Biogeosciences* **6**, 2001–2013 (2009).
9. Jung, M. *et al*. Recent decline in the global land evapotranspiration trend due to limited moisture supply. *Nature* **467**, 951–954 (2010).
10. Jung, M. *et al*. Global patterns of land-atmosphere fluxes of carbon dioxide, latent heat, and sensible heat derived from eddy covariance, satellite, and meteorological observations. *Journal of Geophysical Research - Biogeosciences* **116**, G00J07 (2011).
11. Bonan, G. B. *et al*. Improving canopy processes in the Community Land Model version 4 (CLM4) using global flux fields empirically inferred from FLUXNET data. *Journal of Geophysical Research - Biogeosciences* **116**, G02014 (2011).
12. Draper, C. S., Reichle, R. H. & Koster, R. D. Assessment of MERRA-2 Land Surface Energy Flux Estimates. *Journal of Climate* **31**, 671–691 (2018).
13. Swenson, S. C. & Lawrence, D. M. Assessing a dry surface layer-based soil resistance parameterization for the Community Land Model using GRACE and FLUXNET-MTE data. *Journal of Geophysical Research: Atmospheres* **119**, 10,299–10,312 (2014).
14. Wang, G. *et al*. On the development of a coupled regional climate–vegetation model RCM–CLM–CN–DV and its validation in Tropical Africa. *Climate Dynamics* **46**, 515–539 (2015).
15. Barman, R., Jain, A. K. & Liang, M. Climate-driven uncertainties in modeling terrestrial energy and water fluxes: a site-level to global-scale analysis. *Global Change Biology* **20**, 1885–900 (2014).
16. Rakovec, O. *et al*. Multiscale and Multivariate Evaluation of Water Fluxes and States over European River Basins. *Journal of Hydrometeorology* **17**, 287–307 (2016).
17. Springer, A., Kusche, J., Hartung, K., Ohlwein, C. & Longuevergne, L. New Estimates of Variations in Water Flux and Storage over Europe Based on Regional (Re)Analyses and Multisensor Observations. *Journal of Hydrometeorology* **15**, 2397–2417 (2014).
18. Stegehuis, A. I., Teuling, A. J., Ciais, P., Vautard, R. & Jung, M. Future European temperature change uncertainties reduced by using land heat flux observations. *Geophysical Research Letters* **40**, 2242–2245 (2013).
19. Stegehuis, A. I. *et al*. Summer temperatures in Europe and land heat fluxes in observation-based data and regional climate model simulations. *Climate Dynamics* **41**, 455–477 (2013).
20. Ma, H. Y. *et al*. CAUSES: On the Role of Surface Energy Budget Errors to the Warm Surface Air Temperature Error Over the Central United States. *Journal of Geophysical Research: Atmospheres* **123**, 2888–2909 (2018).
21. Koster, R. D. *et al*. The Pattern Across the Continental United States of Evapotranspiration Variability Associated with Water Availability. *Frontiers in Earth Science* **3** (2015).
22. Tramontana, G. *et al*. Predicting carbon dioxide and energy fluxes across global FLUXNET sites with regression algorithms. *Biogeosciences* **13**, 4291–4313 (2016).
23. Reichstein, M. *et al*. On the separation of net ecosystem exchange into assimilation and ecosystem respiration: review and improved algorithm. *Global Change Biology* **11**, 1424–1439 (2005).
24. Jung, M. & Zscheischler, J. A guided hybrid genetic algorithm for feature selection with expensive cost functions. *Procedia Computer Science* **18**, 2337–2346 (2013).
25. Twine, T. E. *et al*. Correcting eddy-covariance flux underestimates over a grassland. *Agricultural and Forest Meteorology* **103**, 279–300 (2000).
26. Wan, Z. New refinements and validation of the MODIS Land-Surface Temperature/Emissivity products. *Remote Sensing of Environment* **112**, 59–74 (2008).
27. Friedl, M. A. *et al*. MODIS Collection 5 global land cover: Algorithm refinements and characterization of new datasets. *Remote Sensing of Environment* **114**, 168–182 (2010).
28. Myneni, R. B. *et al*. Global products of vegetation leaf area and fraction absorbed PAR from year one of MODIS data. *Remote Sensing of Environment* **83**, 214–231 (2002).
29. Schaaf, C. B. *et al*. First operational BRDF, albedo nadir reflectance products from MODIS. *Remote Sensing of Environment* **83**, 135–148 (2002).
30. Huete, A. *et al*. Overview of the radiometric and biophysical performance of the MODIS vegetation indices. *Remote Sensing of Environment* **83**, 195–213 (2002).
31. Gao, B.-C. NDWI—A normalized difference water index for remote sensing of vegetation liquid water from space. *Remote Sensing of Environment* **58**, 257–266 (1996).
32. Frouin, R. & Murakami, H. Estimating photosynthetically available radiation at the ocean surface from ADEOS-II global imager data. *Journal of Oceanography* **63**, 493–503 (2007).
33. Saigusa, N. *et al*. Impact of meteorological anomalies in the 2003 summer on Gross Primary Productivity in East Asia. *Biogeosciences* **7**, 641–655 (2010).
34. Ueyama, M. *et al*. Change in surface energy balance in Alaska due to fire and spring warming, based on upscaling eddy covariance measurements. *Journal of Geophysical Research: Biogeosciences* **119**, 1947–1969 (2014).
35. Weedon, G. P. *et al*. The WFDEI meteorological forcing data set: WATCH Forcing Data methodology applied to ERA-Interim reanalysis data. *Water Resources Research* **50**, 7505–7514 (2014).
36. Kim, H. *Data Integration and Analysis Systems (DIAS)*, https://doi.org/10.20783/DIAS.501 (2017).
37. Wei, Y. *et al*. The North American Carbon Program Multi-scale Synthesis and Terrestrial Model Intercomparison Project – Part 2: Environmental driver data. *Geoscientific Model Development* **7**, 2875–2893 (2014).
38. Doelling, D. R. *et al*. Geostationary Enhanced Temporal Interpolation for CERES Flux Products. *Journal of Atmospheric and Oceanic Technology* **30**, 1072–1090 (2013).
39. Huffman, G. J. *et al*. Global Precipitation at One-Degree Daily Resolution from Multisatellite Observations. *Journal of Hydrometeorology* **2**, 36–50 (2001).
40. Martens, B. *et al*. GLEAMv3: satellite-based land evaporation and root-zone soil moisture. *Geoscientific ModelDevelopment* **10**, 1903–1925 (2017).
41. Mueller, B. *et al*. Benchmark products for land evapotranspiration: LandFlux-EVAL multi-data set synthesis. *Hydrology and Earth System Sciences* **17**, 3707–3720 (2013).
42. Priestley, C. H. B. & Taylor, R. J. Assessment of Surface Heat-Flux and Evaporation Using Large-Scale Parameters. *Monthly Weather Review* **100**, 81 (1972).
43. Valente, F., David, J. S. & Gash, J. H. C. Modelling interception loss for two sparse eucalypt and pine forests in central Portugal using reformulated Rutter and Gash analytical models. *Journal of Hydrology* **190**, 141–162 (1997).
44. Sachs, L. *Angewandte Statistik: Anwendung Statistischer Methoden*. (Springer, Berlin, 1996).

45. Siemann, A. L., Chaney, N. & Wood, E. F. Development and Validation of a Long-Term, Global, Terrestrial Sensible Heat Flux Dataset. *Journal of Climate* **31**, 6073–6095 (2018).
46. Jung, M. *et al*. FLUXCOM Global Land Energy Fluxes. *Max Planck Institute for Biogeochemistry, Jena*, https://doi.org/10.17871/FLUXCOM_EnergyFluxes_v1 (2018).
47. Trenberth, K. E., Fasullo, J. T. & Kiehl, J. Earth's Global Energy Budget. *Bulletin of the American Meteorological Society* **90**, 311–324 (2009).
48. Miralles, D. G. *et al*. Global land-surface evaporation estimated from satellite-based observations. *Hydrology and Earth System Sciences* **15**, 453–469 (2011).
49. Oki, T. & Kanae, S. Global hydrological cycles and world water resources. *Science* **313**, 1068–1072 (2006).
50. Schlosser, C. A. & Gao, X. Assessing Evapotranspiration Estimates from the Second Global Soil Wetness Project (GSWP-2) Simulations. *Journal of Hydrometeorology* **11**, 880–897 (2010).
51. Miralles, D. G. *et al*. The WACMOS-ET project – Part 2: Evaluation of global terrestrial evaporation data sets. *Hydrology and Earth System Sciences* **20**, 823–842 (2016).
52. Wang-Erlandsson, L., van der Ent, R. J., Gordon, L. J. & Savenije, H. H. G. Contrasting roles of interception and transpiration in the hydrological cycle – Part 1: Temporal characteristics over land. *Earth System Dynamics* **5**, 441–469 (2014).
53. Zhang, K. *et al*. Vegetation Greening and Climate Change Promote Multidecadal Rises of Global Land Evapotranspiration. *Scientific Reports* **5**, 15956 (2015).
54. Jung, M. *et al*. Compensatory water effects link yearly global land CO2 sink changes to temperature. *Nature* **541**, 516–520 (2017).

Acknowledgements

G.C.V. was supported by the European Research Council (ERC) under the ERC Consolidator Grant ERC-CoG-2014 SEDAL (GA 647423). G.T. was supported by the BACI project funded by the EU's Horizon 2020 Research and Innovation Programme (GA 640176). D.P. thanks the support of the RINGO project funded by the EU's Horizon 2020 Programme (GA 703944).

Author Contributions

M.R. and D.P. initiated the FLUXCOM initiative at a RECCAP meeting in Italy in 2010. M.J. coordinated the FLUXCOM initiative, designed the study, and drafted the manuscript. S.K. analysed the results and produced the figures. U.W. helped with data processing. F.G. helped with coding of data processing. K.I. contributed the processing of satellite data and with machine learning code. D.P., G.T., C.S. and G.C.V. contributed machine learning code. M.J., S.K., K.I., D.P., G.T., C.S., G.C.V. and M.R. contributed intellectual input, and edited the manuscript.

Additional Information

Supplementary information is available for this paper at https://doi.org/10.1038/s41597-019-0076-8.

Competing Interests: The authors declare no competing interests.

Publisher's note: Springer Nature remains neutral with regard to jurisdictional claims in published maps and institutional affiliations.